Analysis on the ionospheric scintillation monitoring performance of ROTI extracted from GNSS observations in high-latitude regions

Analysis on the ionospheric scintillation monitoring performance of ROTI extracted from GNSS observations in high-latitude regions

Dongsheng Zhao[a,b], Wang Li[a,b,*], Chendong Li[c], Craig M. Hancock[d], Gethin Wyn Roberts[e,f], Qianxin Wang[a,b]

[a] Key Laboratory of Land Environment and Disaster Monitoring, Ministry of Natural Resources China University of Mining and Technology, Xuzhou 221116, China;

[b] School of Environment and Spatial Informatics, China University of Mining and Technology, Xuzhou 221116, China;

[c] Faculty of Science and Engineering, University of Nottingham Ningbo China, Ningbo 315100, China;

[d] School of Architecture Building and Civil Engineering, Loughborough University, Loughborough Leicestershire LE11 3TU, UK

[e] Department of Land and Sea Mapping, Faroese Environment Agency, Tórshavn, Faroe Islands

[f] Faculty of Natural Sciences and Technology, University of the Faroe Islands, Tórshavn, Faroe Islands

Correspondence: liwang@cumt.edu.cn (W. Li)

Abstract

Monitoring ionospheric scintillation on a global scale requires introducing a network of widely distributed geodetic receivers, which call for a special type of scintillation index due to the low sampling rate of such receivers. ROTI, as a scintillation index with great potential being applied in geodetic receivers globally, lacks extensive verification in the high-latitude region. Taking the phase scintillation index (σ_ϕ) provided by ionospheric scintillation monitoring receivers as the reference, this paper analyses data collected at 8 high-latitude GNSS stations to validate the performance of ROTI statistically. The data is evaluated against 4 parameters: 1, the detected daily scintillation occurrence rate; 2, the ability to detect the daily occurrence pattern of ionospheric scintillation; 3, the correlation between the detected scintillation and the space weather parameters, including the 10.7cm solar flux, Ap, the H component of longitudinally asymmetric and polar cap north indices; 4, the overall distribution of the scintillation magnitude. Results reveal that the scintillation occurrence rates, the occurrence patterns of ionospheric scintillations and the correlations provided by ROTI are generally consistent with those given by σ_ϕ, particularly in the middle-high-latitude region. However, the analysis on the distribution of σ_ϕ for different ranges of ROTI shows ROTI cannot achieve accurate scintillation monitoring at the epoch level in all selected stations. The main outcomes of this paper are of importance in guiding the reasonable application area of ROTI and developing a high-latitude ionospheric scintillation model based on geodetic receivers.

Keywords GNSS; ROTI; Ionospheric scintillation; Geodetic receivers

1 Introduction

Ionospheric scintillation refers to the violent fluctuations in the amplitude or phase of the electromagnetic wave signal passing through ionospheric irregularities (Aarons 1982). Strong scintillation can severely affect the acquisition and tracking process in GNSS receivers, thereby interfering with GNSS positioning navigation and timing (PNT) services. Therefore, it is essential to research techniques to monitor ionospheric scintillation effectively. Due to the continuous and extensive characteristics of GNSS observations, GNSS has been widely used as a critical source of information for ionospheric scintillation monitoring. Dedicated ionospheric scintillation monitoring receivers (ISMR) that are specifically designed to detect scintillations using data collected at 50Hz have become the equipment of choice for ionospheric scintillation monitoring research. However, the high price and substantial memory requirement restrict the distribution of ISMRs, limiting the density of ionospheric scintillation monitoring networks. At present, the ionospheric scintillation monitoring networks mainly include MONITOR (European Union) (Béniguel et al. 2017), CIGALA/CALIBRA (Brazil) (Vani et al. 2017) and CHAIN (Canada) (Jayachandran et al. 2009), deployed with a total of about 150 ISMRs, of which only about 30 stations are located in the Arctic region. Compared to ISMR, geodetic receivers are less expensive and more widely distributed, which is especially the case in the Arctic region. Fig. 1 shows a comparison of the distribution numbers of two type of receivers in the Arctic region of North America, revealing that geodetic receivers can be used to fully monitor the ionospheric scintillation in the land area of the Arctic region. Therefore, to realize the aim of monitoring ionospheric scintillation in large areas, such as the Arctic region, there is a great need to have an investigation of monitoring ionospheric scintillation based on low sampling rate observations by taking advantage of the widely distributed geodetic receivers.

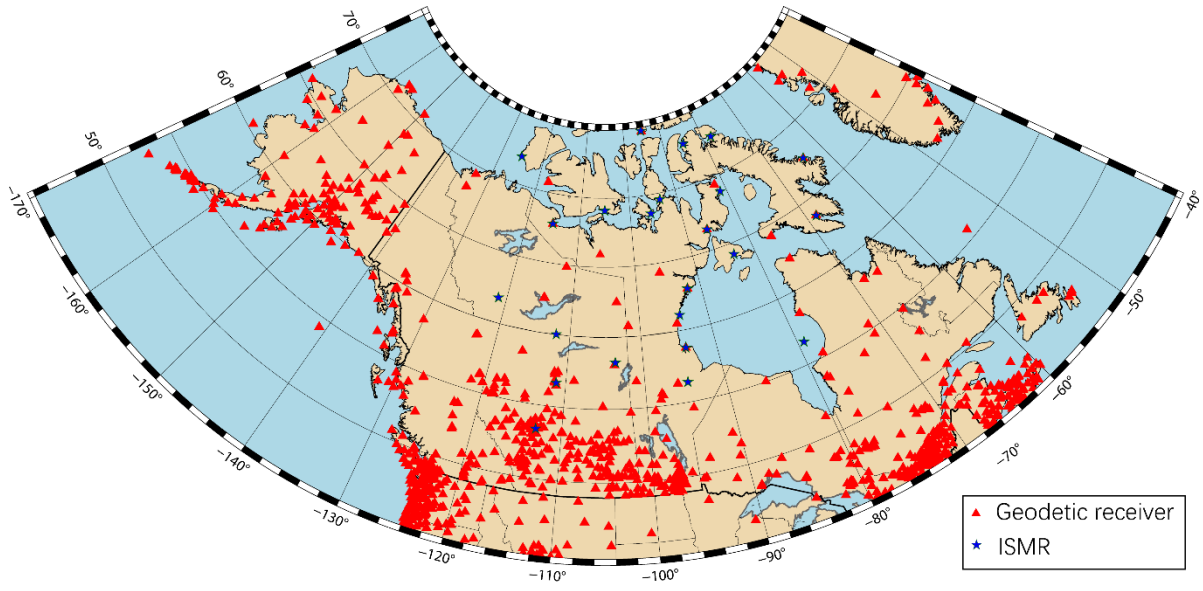

Fig. 1. Comparison of the distribution of geodetic receivers and ionospheric scintillation monitoring receivers in the Arctic region of North America. (Data source: National Oceanic and Atmospheric Administration, Canadian Geodetic Survey, United States Satellite Navigation System and Crust Deformation Observation and Research University Alliance, Canadian High Arctic Ionospheric Network).

During the past decade, several scintillation indices have been proposed based on 1s-sampling-interval observations, making standard geodetic receivers more applicable in monitoring ionospheric scintillations. Due to the scale differences of the ionospheric irregularities that occurred at low and high latitude regions, phase scintillation is more often observed at the Arctic region (Kintner et al. 2007), which is the research interest of this paper. Existing research has proposed several scintillation indices based on geodetic receivers (Luo et al. 2020). Pi et al. (1997) proposed the rate of TEC index (ROTI) based on epoch-differenced carrier phase geometry-free combination; Juan et al. (2018) weighted averaged the ROTI value provided by all the visible satellites in the epoch to generate the along arc TEC rate index (AATR), which has been selected as one of the parameters characterizing ionospheric activity by European Geostationary Navigation Overlapping Service system (EGNOS). Juan et al. (2017) proposed the sigma-ionosphere-free (σ_{IF}) index through using Butterworth filter with 0.1 Hz cutoff frequency to extract ionospheric scintillation signals from the residual of ionosphere-free combination of GNSS carrier phase measurements. Nguyen et al. (2019) extended σ_{IF} index to obtain the scintillation index on each frequency individually by correcting the receiver clock error in each signal. Ahmed et al. (2015) studied the wavelet transform method for extracting ionospheric scintillation signals from VTEC data in high latitude regions. All these scintillation indices were proposed on the basis of 1 Hz sampling rate, while lower sampling rates, e.g. 30s, might challenge the accuracy of these indices.

ROTI attracts the greatest research attention among all the previous proposed scintillation indices. A number of efforts have been made to apply ROTI in studying the variation of ionospheric irregularities over certain regions (Amabayo et al. 2014; ATıCı and SAĞıR 2020), specifically with low latitudes (Carrano et al. 2019; Yang and Liu 2016; Karatay 2020), where the scintillation most frequently occurs. Researches also verified the effectiveness of ROTI in monitoring ionospheric scintillation (Olwendo et al. 2018). Generally, positive correlations can be achieved between ROTI and the scintillation indices provided by ISMR, e.g. both the phase scintillation index (σ_ϕ) and the amplitude scintillation index (S_4) during periods with scintillation activities (Yang and Liu 2016; Pi et al. 2013). Most of the previous studies used observations with 1 Hz or higher sampling intervals. Considering geodetic receivers are mostly set to collecting observations at 30s-sampling-interval, it is more practical to extract the scintillation index from 30s-sampling-interval observations than from 1s-sampling-interval. ROTI can be applied in 30s-sampling-interval data by increasing the period for taking the standard deviation to 5 minutes (Pi et al. 1997). However, the performance of the ROTI from 30s interval still lacks verification, particularly in the high-latitude region.

This paper aims to validate the accuracy of ROTI extracted from 30s-sampling-interval GNSS observations in the high-latitude region by comparing its ionospheric scintillation monitoring performance to that given by σ_ϕ of ISMR. After an introduction to the calculation of the two scintillation indices, e.g. ROTI and σ_ϕ, the two-year observations collected at eight high-latitude stations are adopted to validate ROTI. Then the proper threshold of ROTI in high-latitude regions is briefly discussed, before the scintillation monitoring performance of ROTI is analyzed on account of the following four factors, including the detected daily scintillation occurrence rate, the ability to detect the daily occurrence pattern of ionospheric scintillation, the correlation between the detected

scintillation and the space weather parameters, and the overall distribution of the magnitude. Finally, conclusions are drawn based on the analysis.

2. Introduction to the calculation of ROTI and σ_{ϕ}

2.1 ROTI

2.1.1 Preprocessing strategy of GNSS observations

Preprocessing GNSS observations can improve the data quality (Xiong and Han 2020), which is essential for extracting ROTI. The strategies for preprocessing adopted in this paper include excessive short arc rejection, satellite elevation angle control, and cycle slip detection. As the sliding average window is 5 minutes for ROTI from 30s-sampling-interval observations, it is reasonable to consider and remove any observation arc with less than 100 epochs as the excessive short arc. The satellite cutoff elevation angle is set to 20° to avoid the adverse effects of multipath.

As one of the major error sources affecting the precision of scintillation index, cycle slips need to be detected and corrected in the GNSS observations. For the triple-frequency observations, we adopt the modified Hatch–Melbourne–Wübbena (HMW) combinations with three different signal groups, e.g. (0,1,-1), (1,-6,5) and (4,0,-5) for GPS L1 L2 and L5 respectively. These modified HMW combinations are believed to provide a robust detection and correction performance, where the details refer to Zhao et al. (2019a; 2019b). Most of the geodetic receivers in the Arctic region are still collecting data using only dual-frequency. For these data, we adopt the ionosphere-free (IF) combination to detect cycle slips. The IF combination can reduce the impact of the ionosphere by nearly 99%, thereby providing a detection value precise enough to detect the cycle slips with the magnitude of one or two cycles. However, the IF combination has two main drawbacks. One is the size of the cycle slips cannot be determined directly, making it hard to repair the detected cycle slips. Instead of fixing the cycle slips, the epoch, where a cycle slip is detected, is taken as the start of a new observation arc, to make it be cycle slip free. The second drawback is the IF combination suffers the problem of insensitive cycle slip groups, which means it cannot detect the cycle slips with specific magnitude at L1 and L2 signals (Zhao et al. 2019b). It should be noted that these insensitive cycle slips are really rare in the real observations (Zhao et al. 2019b; Zhao et al. 2021), which should not affect the scintillation index seriously.

2.1.2 Calculation of ROTI

ROTI is currently the most commonly used scintillation index based on low sampling frequency observation data, being used by several researchers in monitoring ionospheric scintillation (Yang and Liu 2016; Li et al. 2018; Cherniak et al. 2018; Yizengaw and Groves 2018; Dugassa et al. 2019). This section will briefly introduce ROTI, together with some detailed processing methods. ROTI is defined as the standard deviation of the rate of TEC (Pi et al. 1997), which can be calculated as follows,

$$STEC(i) = \frac{\Phi_{L1}(i) - \Phi_{L2}(i)}{40.309 \cdot 10^{16} \cdot \left(\frac{1}{f_2^2} - \frac{1}{f_1^2}\right)} \quad (1)$$

$$\mathrm{ROT} = \frac{\mathrm{STEC(i)} - \mathrm{STEC(i-1)}}{T(\mathrm{i}) - T(\mathrm{i-1})} \quad (2)$$

$$\mathrm{ROTI} = \sqrt{\langle ROT^2 \rangle - \langle ROT \rangle^2} \quad (3)$$

where Φ represents the carrier phase measurement in the unit of length; f_1 and f_2 denote the frequency of L1 and L2 signals respectively; T stands for time in the unit of minute; i means the ith epoch; $\langle \cdot \rangle$ denotes the expectation within a certain time interval, which is usually set to 5 minutes for ROTI estimated from 30s-sampling-interval observations. It should be noted that the expectation is calculated using a moving window, making the resolution of ROTI be the same as the sampling interval of the original GNSS observation, namely 30s. ROTI has two main limitations. The first is that ROTI measures the scintillation effect in the geometry-free combination, as can be seen from Eq. (1). The scintillation effects on the signals with different frequencies are not always proportional (Juan et al. 2017; Bhattacharyya et al. 2000), resulting in the scintillation on each individual frequency being unable to be extracted from ROTI. The second is that ROTI will be obliquity with the elevation angle (Fabbro et al. 2019), which means large ROTI values are usually obtained at low elevations. In order to fix this obliquity, we apply a mapping function depending on the satellite elevation angle to ROT (Nguyen et al. 2019), shown as follows,

$$\mathrm{M}(e) = \sqrt{1 - \left(\frac{R_E}{R_E + h} \cdot \cos(e)\right)^2} \quad (4)$$

$$\mathrm{ROTI} = \sqrt{\langle (M \cdot ROT)^2 \rangle - \langle M \cdot ROT \rangle^2} \quad (5)$$

Where ROTI in Eq. (5) flattens the obliquity at low elevation angles; M denotes the mapping function; e is the satellite elevation angle; R_E is the radius of the Earth and h represents the height of the assumed ionospheric layer, which is set to 350 km.

2.2 Phase scintillation index, σ_ϕ

The ionospheric scintillation monitoring receiver (ISMR) is the standard equipment used for ionospheric scintillation monitoring research. The ISMR receivers provide two types of scintillation indices: amplitude scintillation index (S_4) and phase scintillation index (σ_ϕ). Due to the differences in the generation mechanism of ionospheric scintillation in the low latitude and the polar regions, amplitude scintillations often occur in the low latitude region (Jiao and Morton 2015). In contrast, phase scintillations are mainly observed in the polar region (Priyadarshi et al. 2018). Therefore, to reflect the variation information of the scintillation in the high-latitude region, the phase scintillation index will be extensively studied in this paper. The phase scintillation index provided by ISMR, namely σ_ϕ, can be calculated as follows,

$$\sigma_\phi = \sqrt{\langle \phi^2 \rangle - \langle \phi \rangle^2} \quad (6)$$

where ϕ represents the detrended carrier phase measurement. In the process of calculating the expectation of σ_ϕ, the time interval is set to 60s and the moving window is not adopted. Since ISMR has the ability to collect

observations at 50 Hz, a sixth-order Butterworth filter with 0.1 Hz cutoff frequency can detrend the raw carrier phase measurements precisely (Van Dierendonck et al. 1993), thereby providing highly accurate phase scintillation index, which can be adopted as the reference value to measure the accuracy of the scintillation index extracted from observations with 30s sampling rate. 0.2 rad/min is selected as the threshold of σ_ϕ to indicate the occurrence of scintillation activities.

3. Introduction to the adopted data

Canadian High Arctic Ionospheric Network (CHAIN) is a distributed array of ground-based GNSS stations located in the Canadian high Arctic region, with a scientific object to understand scintillation producing structures particular in the polar cap region, a region of open magnetic field lines (Jayachandran et al. 2009). CHAIN has 25 high data-rate GNSS Ionospheric Scintillation and Total electron content monitors (GISTM), of which only 14 monitors are equipped with the Septentrio PolaN GG antenna and the Septentrio PolaRxS Pro ionospheric scintillation monitoring receiver, which can log out ionospheric scintillation monitoring file, containing the phase scintillation index σ_ϕ. This paper selects 8 stations evenly distributed among them to validate the ionospheric scintillation monitoring performance of ROTI extracted from 30s-sampling-interval observations in the high-latitude region, as shown in Fig. 2. Four stations, namely arcc, sacc, kugc and repc are located in the polar cap region, while the other four stations, namely fsmc, ranc, chuc and mcmc, are located in the middle-high-latitude region. All the receivers are set to collect dual-frequency GPS observations at 50 Hz sampling rate to calculate the phase scintillation index σ_ϕ, which is taken as the reference for the comparison. Observations collected during years of 2019 and 2020 are adopted in this paper. The observation files filtered into 30s-sampling rate are also obtained to generate ROTI.

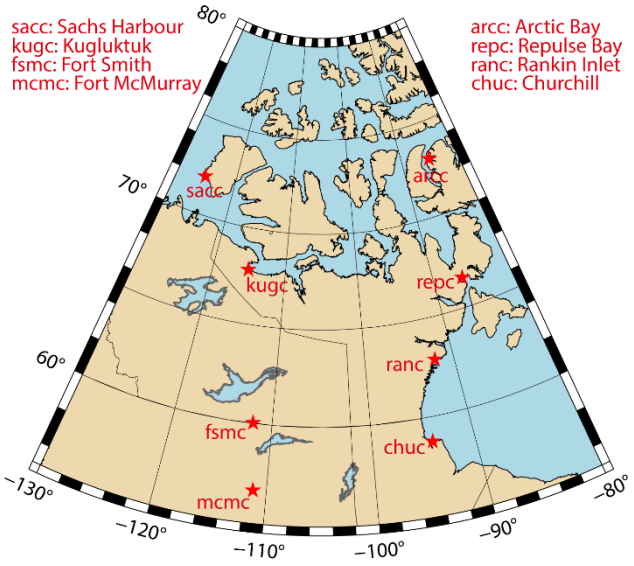

Fig. 2. Distribution of the adopted stations, with their full names and abbreviations.

4. Scintillation monitoring performance of ROTI

This section will analyze the scintillation monitoring performance of ROTI utilizing the two-year observations from 8 high-latitude stations. After a brief discussion about the threshold of ROTI in high-latitude regions, the performance of ROTI is evaluated with regards to the following four factors, including the detected daily scintillation occurrence rate, the ability to detect the daily occurrence pattern of ionospheric scintillation, the correlation between the detected scintillation and the space weather parameters, and the overall distribution of the magnitude. If the above four factors provided by ROTI are consistent with those of the reference, it is reasonable to believe ROTI extracted from observations with 30s-sampling-interval can monitor the ionospheric scintillation reliably in the high-latitude region. It is worth mentioning that the phase scintillation index given by the ISMR L1 carrier is adopted as the reference in this paper, as the scintillation effects on GPS L1 and L2 are basically proportional with nearly the same magnitude in the high-latitude region (Jiao and Morton 2015).

4.1 Threshold of ROTI in high-latitude regions

The experience value for the threshold of ROTI in high-latitude regions is still a controversial question. 0.2 TECU/min is usually adopted as the threshold of ROTI (Pi et al. 1997), especially for the observations collected in low latitude regions. In high latitude regions, the increase of the Fresnel frequency and the scope of ionospheric irregularities challenge the applicability of 0.2 TECU/min as the threshold. To test the applicability of 0.2 TECU/min and select the proper threshold of ROTI in high-latitude regions, we conduct a discrete comparison with threshold values ranging from 0.2 to 0.7 in steps of 0.05, on account of the following three factors, namely the correlation of the daily ionospheric scintillation occurrence rates between ROTI and the reference, the mean and the standard deviation of the rate difference between ROTI and the reference. The ionospheric scintillation occurrence rate (R) is defined as follows,

$$\mathrm{R} = \frac{N_S}{N} \times 100\% \tag{7}$$

where N_S denotes the total number of epochs where the ionospheric scintillation index is above the threshold within a certain period of time; N is the total number of epochs within a certain period of time. For calculating the daily ionospheric scintillation occurrence rate, the period is set to 24 hours in Eq. (7). The time resolution for σ_ϕ is 60s, while ROTI has a 30s resolution, which needs to be re-sampled into 60s for easy comparison. Correlation reflects the similarity of the two scintillation monitoring results, while the mean value reflects the deviation of the occurrence rate provided by ROTI compared to the reference, and the standard deviation reflects the dispersion of the rate difference. The selection criteria of a proper threshold should be the one providing a similar occurrence rate to the reference, with no deviation and small dispersion, which means a high correlation with a small standard deviation and a zero-mean value.

Fig. 3 displays the variation of the correlation, mean and standard deviation with different thresholds, where the selected suitable threshold for each station is marked with a cyan vertical line. Results show that it is usually difficult to select a threshold which meets well with the selection criteria, thus the selection of the proper threshold for each station is based on experience, described as follows. For the four stations located in the polar cap region, namely arcc, sacc, kugc and repc, false alarms of ROTI caused by the strict threshold can be significantly avoided

with the increase of the threshold, which brings the increase of correlation and the decrease in both the mean and standard deviation. Thus, the proper thresholds for these four stations can be easily selected as the ones providing highest correlations, namely 0.5, 0.5, 0.35 and 0.4 (TECU/min) for arcc, sacc, kugc and repc respectively. For ranc station, the threshold with the highest correlation has a negative mean value and a large standard deviation, indicating it might lead to too many missed scintillation alarms. Thus, the proper threshold for ranc station is selected as 0.35 TECU/min, which can provide a zero mean and the smallest standard deviation. For stations fsmc, chuc and mcmc, the correlation will decrease with the increasing threshold value, while the 0 mean value and the smallest standard deviation are both obtained at 0.25 TECU/min, which is selected as proper threshold for these three stations. This figure also shows that the proper threshold gradually changes from 0.25 TECU/min to 0.5 TECU/min with the increase of the latitude, revealing that the threshold for high-latitude regions is different from that for low-latitude regions. This is consistent with Ma and Maruyama (2006), who suggest the 0.5 TECU/min to indicate the presence of ionospheric irregularities at a length of a few kilometers in polar cap regions. It can be seen from the figure that the correlation generally grows with the decrease of the latitude, revealing that ROTI can provide a more accurate daily scintillation occurrence rate at the middle-high-latitude stations.

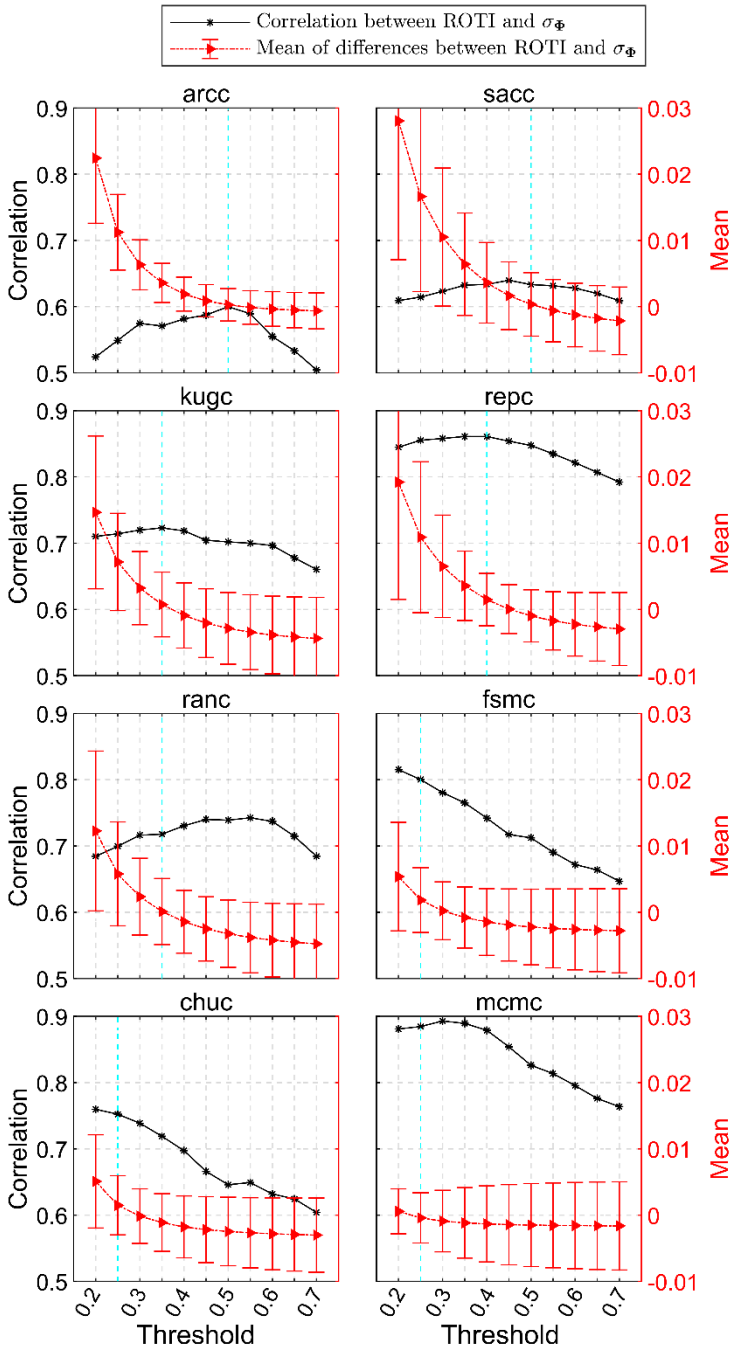

Fig. 3. Correlation of the daily ionospheric scintillation occurrence rates between ROTI and ISMR, the mean and the standard deviation of the rate difference between ROTI and ISMR for different thresholds. The standard deviation is displayed as the error bar. The panels are sorted in descending order of latitude from top to bottom, which is applied to all the following figures.

4.2 Detected daily scintillation occurrence rate

The left four panels of Fig. 4 and Fig. 5 present the daily ionospheric scintillation occurrence rate obtained by σ_ϕ and ROTI from the eight stations respectively, while the right panels show the distributions of the occurrence rate differences between ROTI and σ_ϕ. For comparing detection performance, results given by the thresholds selected

in Section 4.1 and 0.2 TECU/min are both displayed in the two figures. The daily ionospheric scintillation occurrence rates given by 0.2 TECU/min is generally higher than that of ISMR during the two-year period at all the 8 stations, making the distribution of the corresponding daily rate differences have a positive skew. False alarms caused by the strict threshold can be significantly decreased by adopting the selected thresholds at all the 8 stations, making 80% of the daily scintillation occurrence rate difference be concentrated at $\pm 0.05\%$. This further reveals that the threshold value, 0.2 TECU/min, determined in the low-latitude region, is not applicable in the high-latitude region. A better scintillation monitoring performance of ROTI can be achieved with the thresholds selected in this paper. The daily scintillation occurrence rate is only a necessary condition, but not a sufficient condition, to confirm scintillation detection performance of ROTI. The scintillation detection ability of ROTI at the hourly level, scintillation occurrence pattern level and epoch level will be furtherly discussed in Sections 4.3, 4.4 and 4.5 respectively.

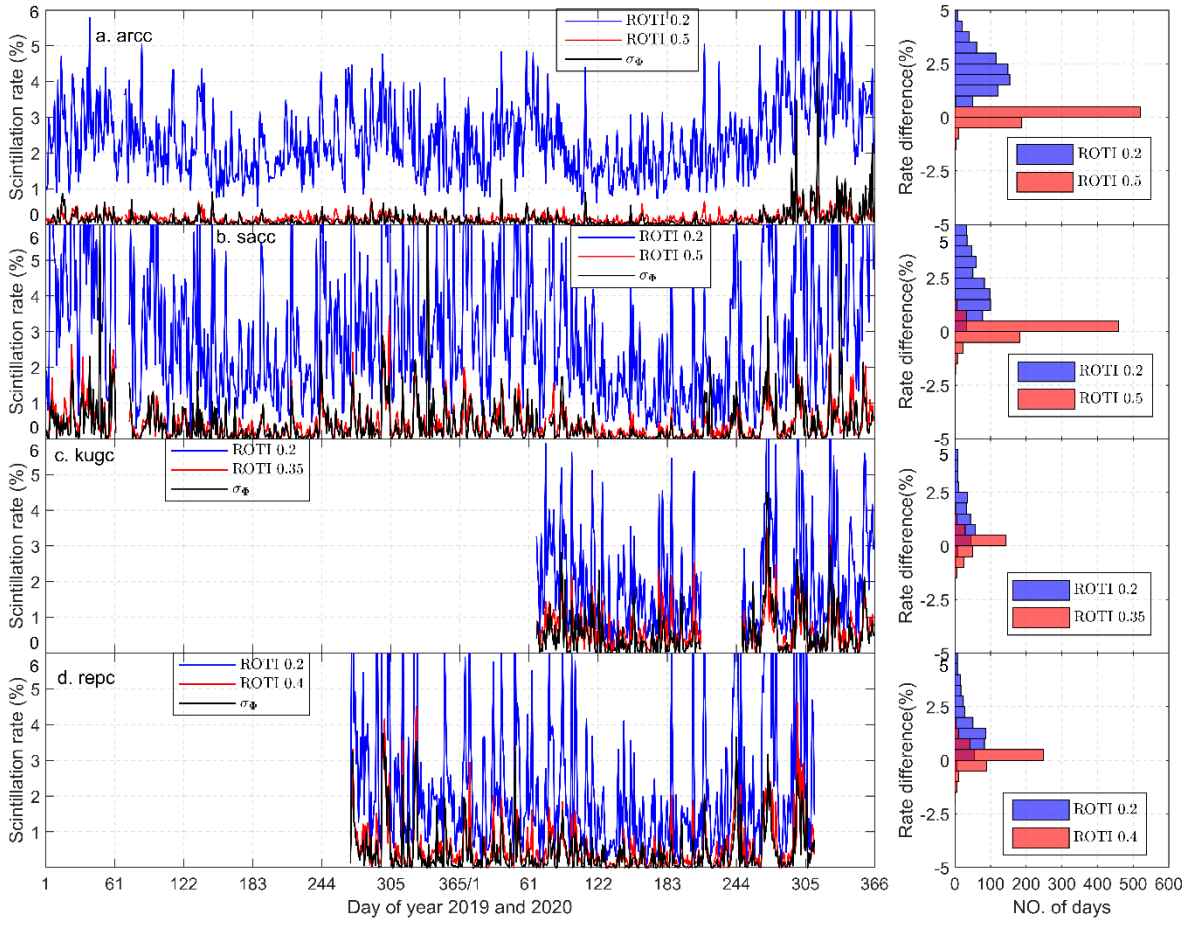

Fig. 4. Ionospheric scintillation occurrence rate provided by ROTI and σ_ϕ at arcc, sacc, kugc and repc stations. The left four panels show the occurrence rate during the two-year period, while the right four panels show the rate difference between ROTI and σ_ϕ. The numbers in the legend indicate the threshold of ROTI in the unit of TECU/min. Clock failures are witnessed at sacc during days 63 to 72 in 2019, kugc during the whole year of 2019 and days 1 to 66, 214 to 248 in 2020, repc during days 1 to 268 in 2019. Periods with clock failure or no observations are not displayed in this figure. The observations during the clock failure period are not adopted in the analysis of this paper.

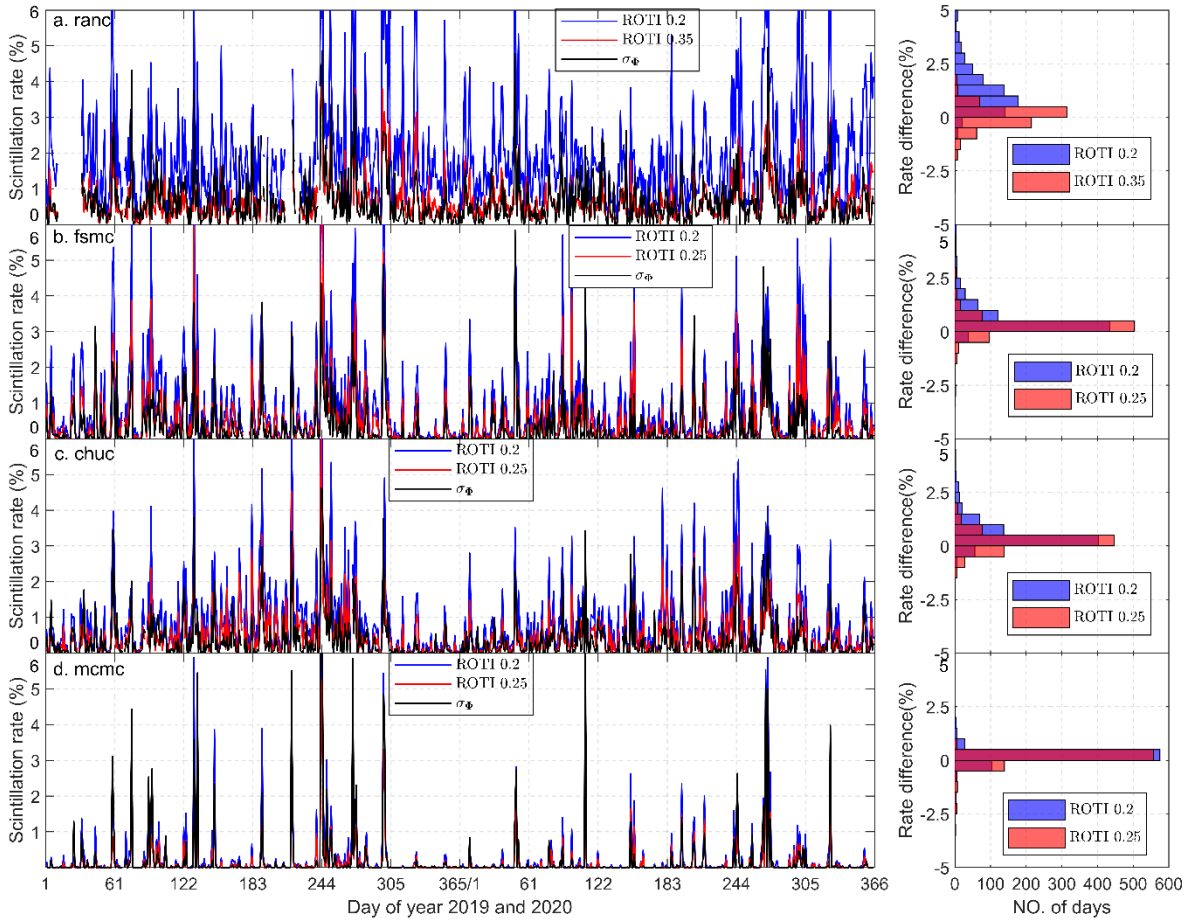

Fig. 5. Same as Fig. 4, but for ranc, fsmc, chuc and mcmc stations.

4.3 Detecting the daily occurrence pattern of ionospheric scintillation

Existing studies have shown that the occurrence of ionospheric scintillation has the characteristic of diurnal dependency, which is partly related to the local solar angle (Alizadeh et al. 2020). This section will evaluate the performance of ROTI at hourly level in detecting this local-solar-angle depended characteristic according to the following procedures. Firstly, the local sunset and sunrise time are calculated based on latitude and longitude of the station utilizing the astronomical algorithms proposed by Meeus (1998) with regards to the correction of Atmospheric Refraction Effects (ARE), shown as follows,

$$ARE = \frac{1^\circ}{3600''}\left[\frac{58.1''}{\tan(h)} - \frac{0.07''}{tan^3(h)} + \frac{0.000086''}{tan^5(h)}\right] \quad (8)$$

Where, h stands for Solar elevation angle in the unit of degree. The sunrise and sunset time calculated here are at the ground height, instead of the ionospheric height, which might reflect the influence of the local solar angle on scintillation more directly. However, the focus of this paper is to compare the diurnal variation difference of ionospheric scintillations between ISMR and ROTI, making it be able to ignore the effect of the estimation altitude on solar hour angle. The atmospheric pressure, humidity and other variables not considered in this paper can also lead to the inaccuracy of the estimated time. This inaccuracy is on the minute level, while the ionospheric scintillation characteristics detected by the scintillation factor analyzed in this article are on the hour level,

therefore it is reasonable to believe that the estimated sunrise and sunset time are precise enough to be used to analyze the occurrence pattern of scintillation. The calculated sunrise and sunset time are converted to GPS time according to the time zone where each station is located. Then, we calculate the scintillation occurrence in each hour after the sunrise or sunset. Lastly, the ratio of the number of epochs with scintillation in each hour over the total number of epochs with scintillations within years of 2019 and 2020, which is called scintillation occurrence probability in this paper, will be used to study the diurnal scintillation characteristic. Due to the high latitude, arcc, sacc and kugc stations witness polar day and polar night phenomena every year, during which the distribution of ionospheric scintillation is analyzed separately according to the local time.

Fig. 6 presents the occurrence of ionospheric scintillation after local sunset. According to the occurrence characteristic provided by ISMR, one peak can be clearly observed at arcc station within 6 hours before sunset, while the peaks observed at the middle-high-latitude stations, e.g. ranc, fsmc and chuc, occur within 6 hours after sunset. The mcmc station witnesses this peak in 6 to 12 hours after sunset. The sacc, kugc and repc stations witness lower scintillation occurrence rates than other stations. Besides that, scintillations can occur at any time of the day at sacc, kugc and repc stations. The daily scintillation occurrence rates provided by ROTI are basically in compliance with those given by ISMR, especially at arcc, sacc and chuc stations, while those at mcmc and ranc stations are lower than the reference, and that at fsmc station is higher than the reference. The above phenomenon could be resulted from many reasons. To the best of the authors' knowledge, we think the reasons could lie in the following aspects. Firstly, ROTI is estimated from GPS observations with 30s interval, while σ_ϕ is obtained from the observations with 50 Hz. Observations with 30s sampling rate can only detected the ionospheric irregularities with scale sizes in the order of 30 km (Pi et al. 1997). Any irregularity lower than 30 km will not be alarmed by ROTI, leading to the lower scintillation occurrence rate. Secondly, the threshold for cycle slip detection in calculating ROTI is challenging to distinguish between scintillation and cycle slips during the period with strong scintillation. The excessive phase scintillations are treated as cycle slips, which causes the estimated amplitude of the strong scintillation to be lower than the reference, leading to the decrease in the proportion of the high-amplitude scintillation. Thirdly, ROTI extracted from 30s-sampling-interval observations is affected by unmodelled and un-eliminated errors, decreasing the accuracy of ROTI. Fourthly, ROTI estimated the gradient variation of the slant total electron content of the ionosphere, which is not completely consistent with the ionospheric scintillation. The above four reasons are only the authors' conjecture on the inconsistency of scintillation occurrence rates between ROTI and σ_ϕ. Since this paper focuses on detecting this inconsistency to evaluate the reliability of ROTI in monitoring scintillation, the specific reasons leading to this inconsistency are left for future research.

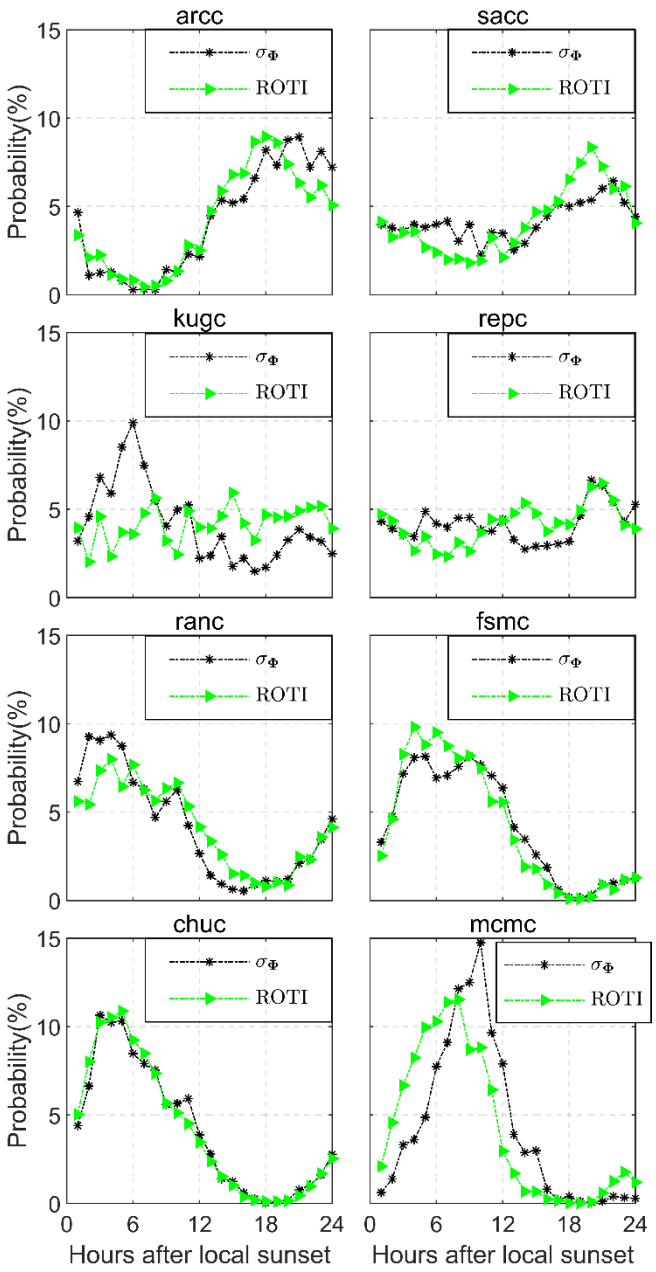

Fig. 6. Scintillation occurrence probability with respect to hours after local sunset.

Fig. 7 shows the occurrence of ionospheric scintillation after sunrise. The occurrence pattern provided by ISMR is similar to that after local sunset. One occurrence peak can be observed at arcc, ranc, fsmc, chuc and mcmc stations, while sacc, kugc and repc stations can witness the occurrence of scintillation equally at each hour of a day. The peak at arcc station is observed within 6 hours after local sunrise, while ranc, fsmc, chuc and mcmc stations witness their peaks approximately 6 hours before local sunrise. Compared to Fig. 6, peaks related to sunrise are generally higher than those related to sunset, which might be due to solar radiation. ROTI can basically detect all the above phenomenon, except the magnitudes of the peaks at arcc, ranc and mcmc stations are a little lower than the reference.

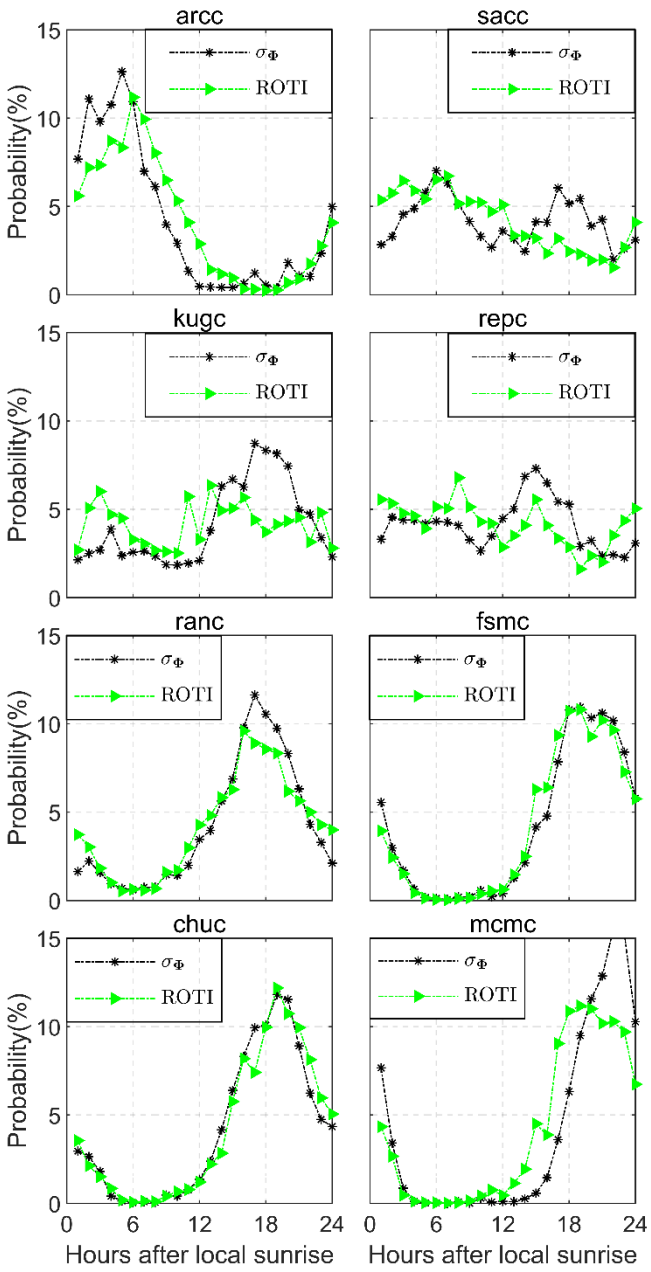

Fig. 7. Scintillation occurrence probability with respect to hours after local sunrise.

Fig. 8 and Fig. 9 show the occurrence of ionospheric scintillation during the period of polar day and night respectively. Fig. 9 does not list the results from repc, as no obvious polar night phenomenon occurred at repc station in years of 2019 and 2020, due to its latitude. The ionospheric scintillation occurrence rates have similar pattern during both polar days and nights, with one peak observed at arcc station and no obvious peak for the other stations. The probabilities of the scintillation at sacc, kugc and repc stations may occur throughout the day and are much lower than that at arcc station. Compared between Fig. 8 and Fig. 9, it can be seen that the peak value of the arcc station during the polar day is higher than that during the polar night, which might be due to the effect of solar radiation of polar day. ROTI can provide a similar ionospheric scintillation occurrence rate to the reference

at sacc, kugc and repc stations. The peak obtained at arcc station is obviously lower than the reference, illustrating that ROTI is not suitable for ionospheric scintillation monitoring in the polar cap region.

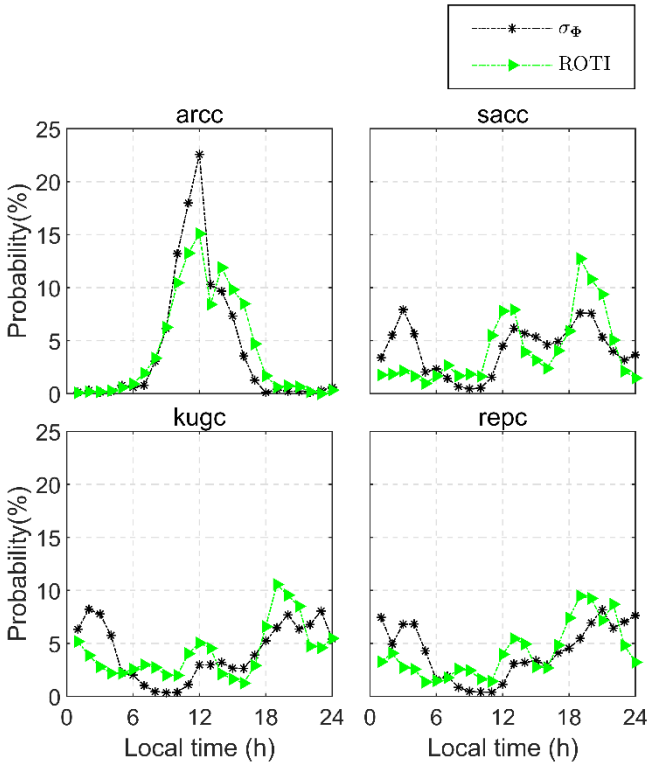

Fig. 8. Scintillation occurrence probability during Polar day.

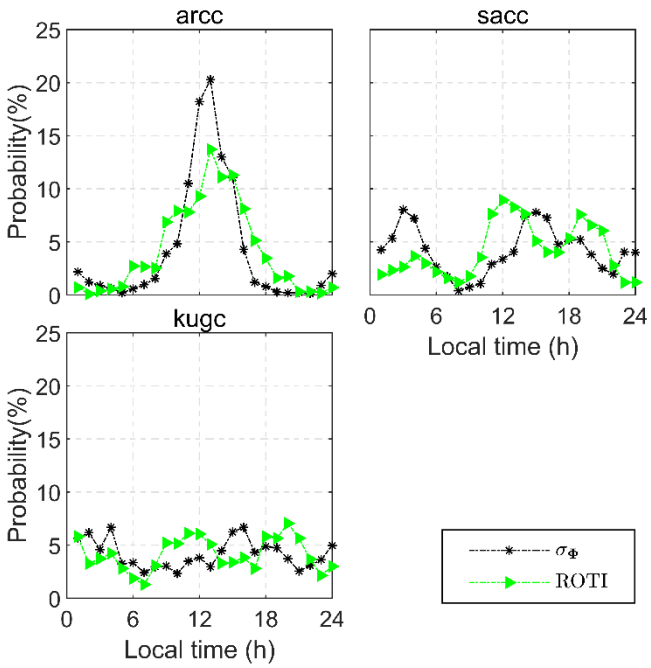

Fig. 9. Scintillation occurrence probability during Polar night.

4.4 Correlation between the scintillation detection rate and the space weather parameters

Space weather refers to conditions on the sun and in the solar wind, magnetosphere, ionosphere, and thermosphere that can influence the performance and reliability of space-borne and ground-based technological systems and can endanger human life or health (Khazanov 2016). As a result of space weather disturbances, the electron density of the ionosphere along receivers' line-of-sight varies rapidly, causing ionospheric scintillation. The space weather conditions are represented by the 10.7cm solar flux (F10.7), Kp/Ap, the H component of longitudinally asymmetric (ASY-H) and polar cap north (PCN) indices in this paper, as shown in Fig. 10. The 10.7cm Solar Flux represents the integrated emission at 10.7cm wavelength from all sources present on the disc, proving to have a linear correlation with the total photospheric magnetic flux, a direct manifestation of solar activity. The 10.7cm Solar Flux values adopted in this paper are measured by two fully automated radio telescopes, located at the Dominion Radio Astrophysical Observatory, which provides three flux determinations each day at 17:00, 20:00 (local noon) and 23:00UT between March and October, and 18:00, 20:00 and 22:00UT during the rest of the year. The Kp/Ap index is provided with a resolution of three-hour, measuring solar particle radiation by its magnetic effects (Matzka et al. 2020). The years of 2019 and 2020 are at the end of the 24th and the beginning of the 25th solar cycle respectively. The F10.7 index fails to be provided on the 261st day of 2019, which is omitted in the following analysis. According to the top panel of Fig. 10, nearly the whole year of 2019 and about the first three quarters of 2020 have calm solar activities, while three peaks of F10.7 index are observed on the day 311, 334 and 357 of 2020. The peak on the day 311 of 2020 is due to coronal mass ejection, while the day 334 of 2020 has the largest F10.7 index for the reason that the coronal mass ejection was occurred with a M level X-ray flare. Day 357 of 2020 has disturbed geomagnetic activity, as shown in the second panel of Fig. 10. The most disturbing geomagnetic activity occurred on the day 269 of 2020, in which the magnitude of Kp reached 6. For high latitude regions, another important index to indicate space weather condition is the Auroral Electrojet (AE) index, which is derived from geomagnetic variations in the horizontal component observed at 10 to 13 observatories along the auroral zone in the northern hemisphere and designed to provide a global, quantitative measure of auroral zone magnetic activity produced by enhanced Ionospheric currents flowing below and within the auroral oval (Davis and Sugiura 1966). Thus, AE is considered to have a direct consequence in the generation of ionospheric scintillations. As the values of the AE index after March, 2018 were derived from unverified raw data, they are inaccurate and not provided in the digital format. To describe the ionospheric variation in the high-latitude regions during years of 2019 and 2020, this paper adopts the following two indices, ASY-H index and PCN index. Although ASY-H index is designed to measure the geomagnetic disturbance fields in mid-latitudes, it has been shown that ASY-H correlates well with the AE index (Crooker 1972; Clauer and McPherron 1980). Compared to AE index, ASY-H are more smoothly varying and difficult to reflect minor sub-storm activity. To reduce the adverse effect of this difference, the daily averaged ASY-H is adopted in the analysis. The PCN index is designed to monitor the polar cap magnetic activity generated by the geoeffective solar wind parameters, thus it can be used as a measure of the ionospheric condition in high-latitude regions.

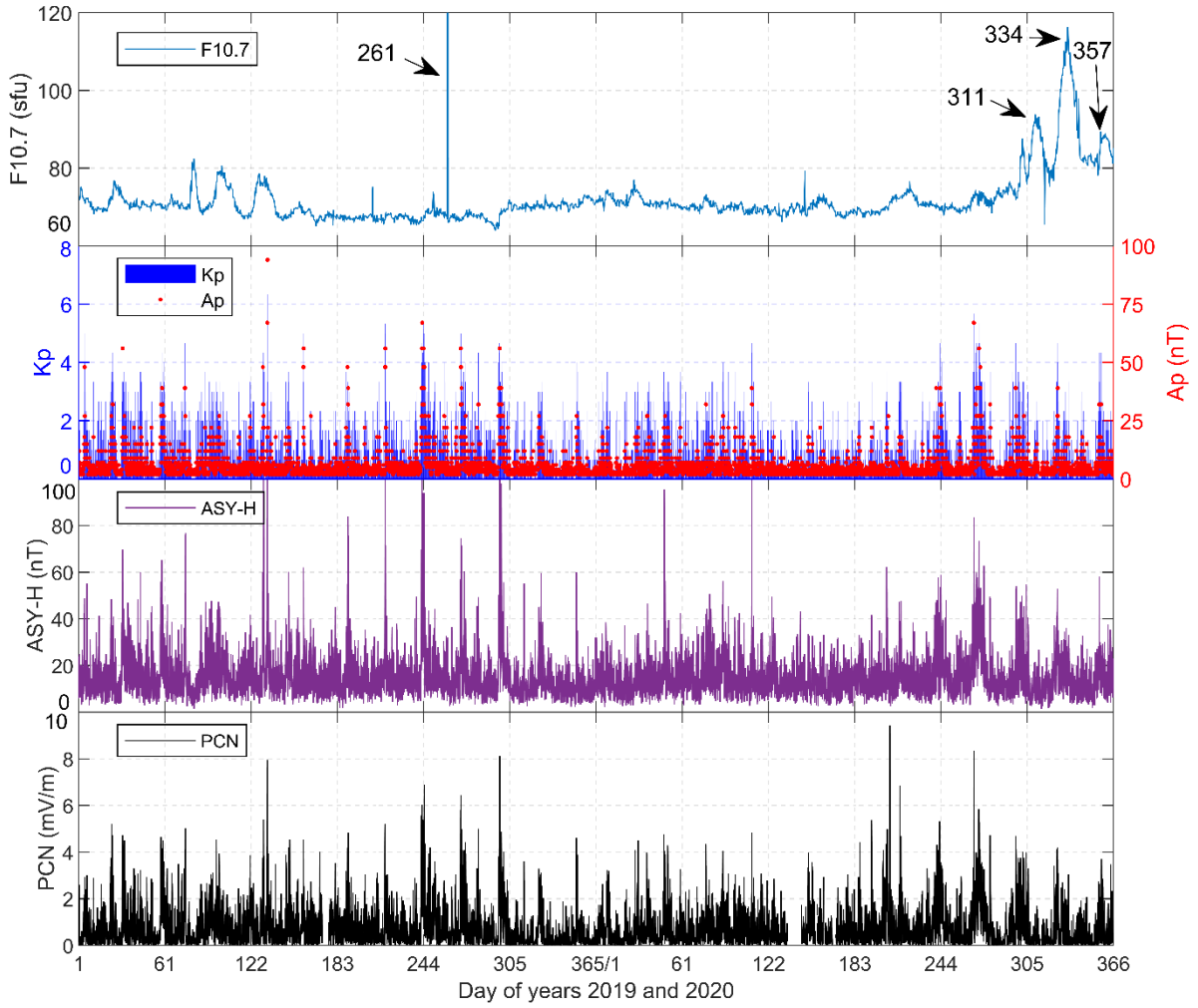

Fig. 10. Space weather condition in years of 2019 and 2020. sfu stands for solar flux units (1 sfu = 10^{-22}Wm^{-2}Hz^{-1}).

Ionospheric scintillation is closely related to interplanetary magnetic fields and geomagnetic field disturbances, especially in the high-latitude region (ALIZADEH et al. 2020). The correlation between the detected scintillation rate and the parameters of space weather condition, e.g. F10.7 and Ap, can be further adopted to evaluate the performance of ROTI, as the correlation given by ROTI should be similar to that of ISMR if ROTI can monitor high-latitude scintillations accurately. The scatter diagram in Fig. 11 presents the distribution of the daily ionospheric scintillation occurrence rate with regards to the daily averaged F10.7 index, while the straight lines in this figure are the least square fit to the distribution of the corresponding scintillation index in order to reveal the correlation between the scintillation index and the daily averaged F10.7 index. The corresponding values of the correlation are listed in each subpanel. Since F10.7 index is biased distributed between 60 and 120 sfu, which will affect the calculation of the correlation. To solve this problem, the F10.7 index is normalized between 0 and 1. From the results of ISMR, a weak positive correlation can be obtained between the daily scintillation occurrence rate and the F10.7 index at arcc and sacc station, while nearly no correlation or even negative correlation can be achieved for the other stations. This might be because that the magnetic field intensity is almost zero in the polar

cusp region, where arcc and sacc stations are located, allowing the solar wind to enter the upper atmosphere of this region unimpeded. After the solar wind hit the Earth's magnetosphere initially by electromagnetic radiation and later by the solar particles, charged particles from the solar wind and magnetosphere, mostly electrons and protons, precipitate in the upper atmosphere and dissipate their energy by generating the auroral emission (Jin et al. 2014; van der Meeren et al. 2015; Priyadarshi et al. 2018). Due to this solar wind-magnetosphere-ionosphere coupling, strong ionospheric scintillations are observed in the polar cusp regions. Compared to the auroral scintillations, the cusp region scintillations are usually long lasting, which is associated with the ionospheric irregularity perturbation in the cusp region as well as cusp region particle precipitation (Prikryl et al. 2015; Jiao et al. 2013). This might be a reason why a higher correlation can be obtained at arcc and sacc stations in this figure. In middle-high-latitude regions, the ionospheric scintillation is greatly affected by the geomagnetic field, making the daily scintillation occurrence rates do not show a strong correlation with the F10.7 index. The figure also shows that ROTI obtains a correlation similar to the ISMR scintillation index, indicating ROTI can detect the scintillation caused by solar wind.

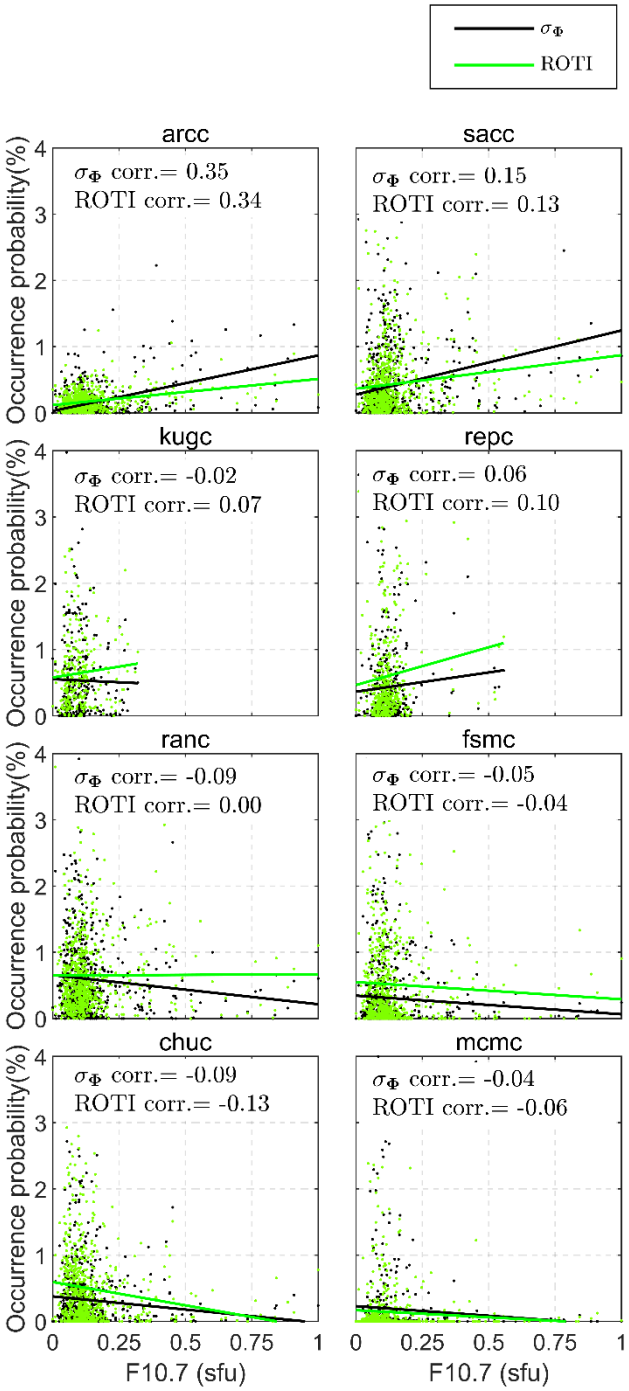

Fig. 11. Distribution of scintillation daily occurrence rate and its least square fitted lines with regards to the daily averaged and yearly normalized F10.7 index.

The scintillation monitoring performance of ROTI is studied by considering the relationship between the ionospheric scintillation daily occurrence rate and the daily averaged Ap index, as presented in Fig. 12, while the values of the correlations are listed in each panel of the figure. It can be seen from the results of ISMR that the correlations at arcc and kugc stations are much lower than those given by the other stations, which can generally be above 0.7. This phenomenon is opposite to the correlation performance involving with F10.7. Generally, ROTI

can provide correlations similar as ISMR at nearly all the stations, revealing ROTI can detect the scintillations caused by geomagnetic activities.

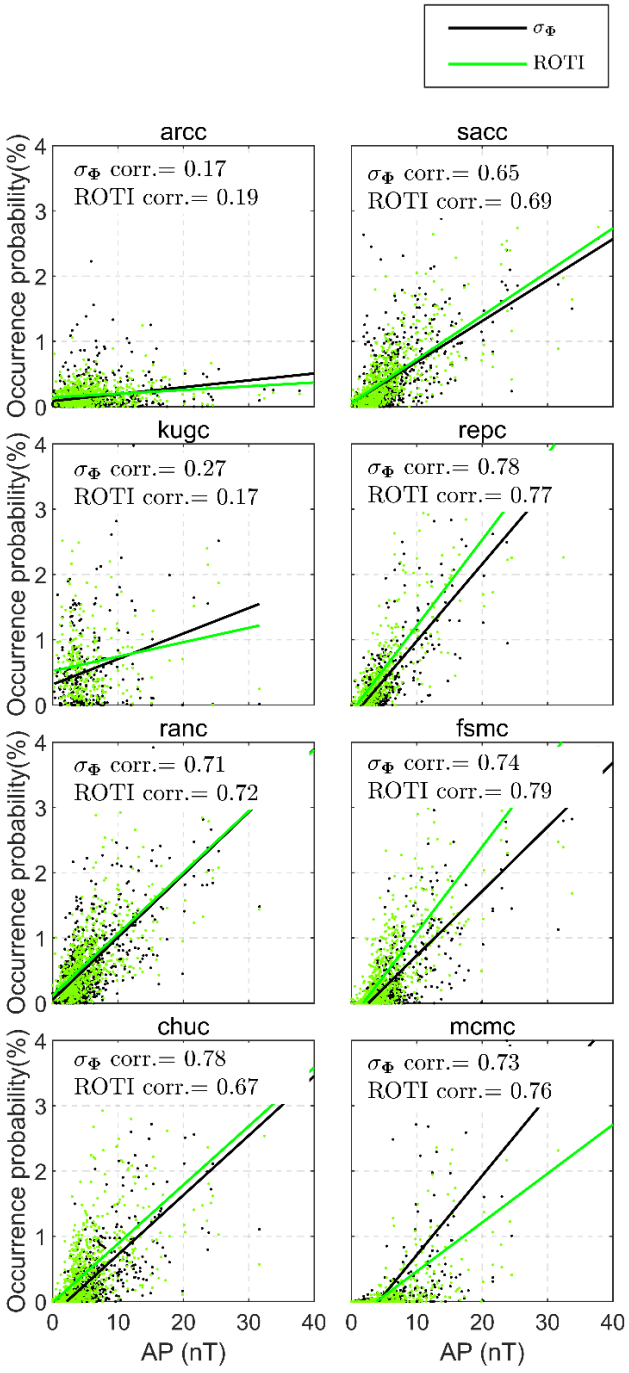

Fig. 12. Distribution of scintillation daily occurrence rate and its least square fitted lines with regards to the daily averaged Ap index.

The scintillation monitoring performance of ROTI is further studied by considering the relationship between the ionospheric scintillation daily occurrence rate and the daily averaged ASY-H and PCN indices, of which the results are shown in Fig. 13 and Fig. 14 respectively. Similar to the results with Ap, a high correlation about 0.7

can be achieved at nearly all the stations except for arcc and kugc. The main focus of this study is on the similarities and differences between the correlations obtained by ROTI and σ_ϕ. The similar correlation can indicate that the scintillations detected by both ROTI and σ_ϕ are driven by the same sources. On the contrary, the scintillation given by ROTI might be interfered by other factors, such as multipath. Similarly, readers can verify the accuracy of ROTI by calculating the correlation between the scintillation occurrence rate and various factors, e.g. IMF By, Bz etc. Due to the limitation of the paper length, no further verification and analysis is performed here.

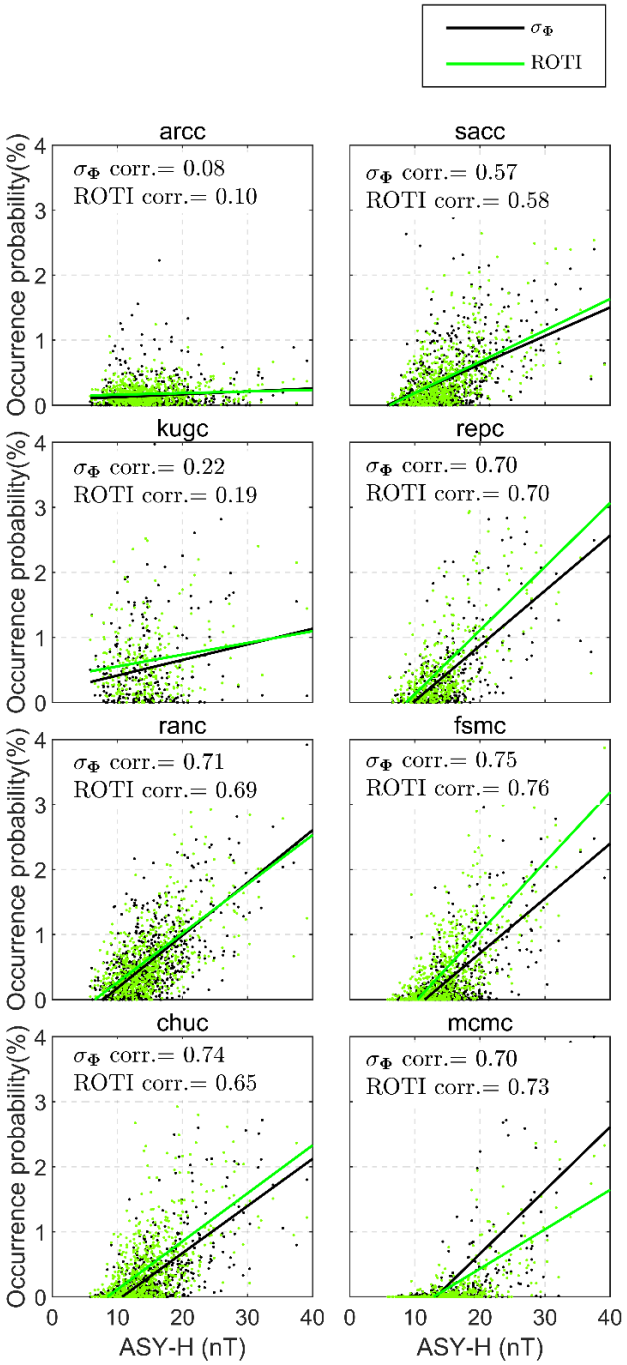

Fig. 13. Distribution of scintillation daily occurrence rate and its least square fitted lines with regards to the daily averaged ASY-H index.

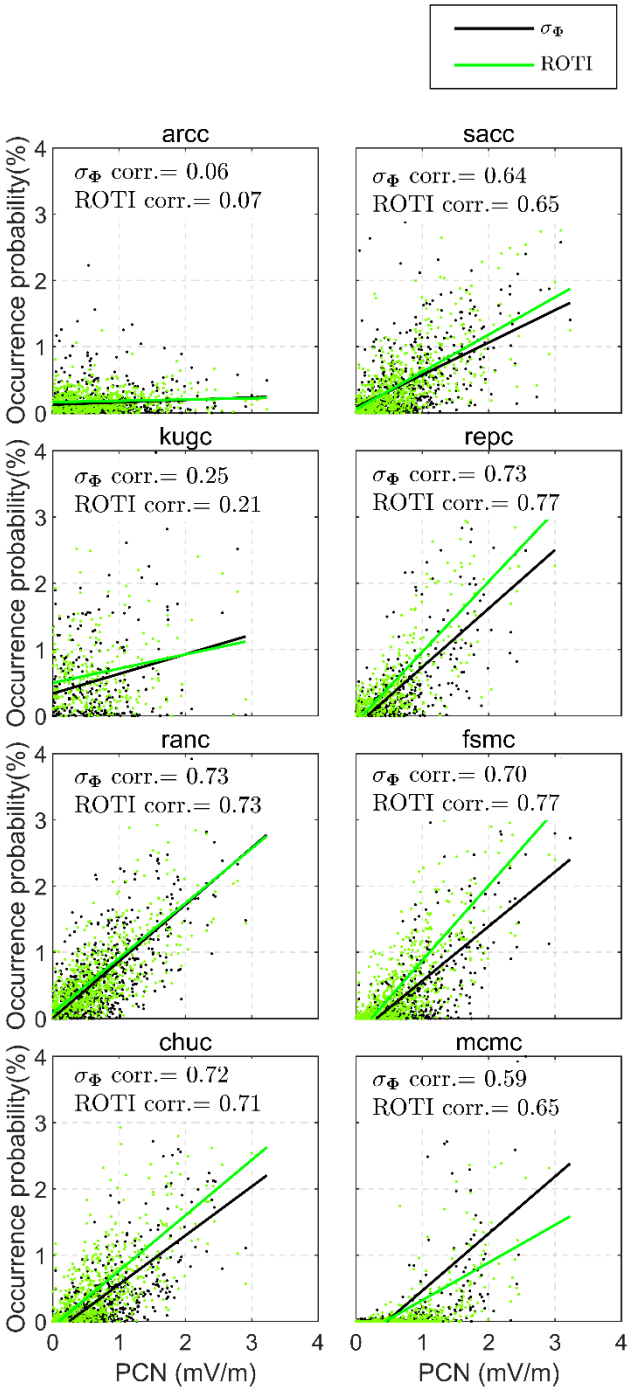

Fig. 14. Distribution of scintillation daily occurrence rate and its least square fitted lines with regards to the daily averaged PCN index.

4.5 Distribution of the magnitude

Apart from the scintillation occurrence rate, the accuracy of the estimated magnitude of scintillation is another factor to measure the performance of ROTI in monitoring ionospheric scintillation, thus this section will discuss the distribution of the magnitude. Fig. 15 presents distribution of the magnitude of scintillation indices above the corresponding thresholds in the two years. The different starting points of x-axis for ROTI and σ_ϕ are due to the

adoption of different thresholds. It can be seen that the distribution of both ROTI and σ_ϕ over the thresholds approximately conforms to the logarithmic function. The distribution given by ROTI at the stations ranc, fsmc, chuc and mcmc, matches well with that given by ISMR, while the proportion of low-magnitude scintillation is significantly lower than the reference value at the other four stations, especially at arcc and sacc. The reason might be that the ionosphere varies more drastically in the high-latitude region than that in the middle-high latitude region, leading to a more drastic variation gradient of the slant total electron content measured by ROTI. Thus, it is easy for ROTI to provide larger scintillation alerts in the high-latitude region, decreasing the accuracy of ROTI in such region.

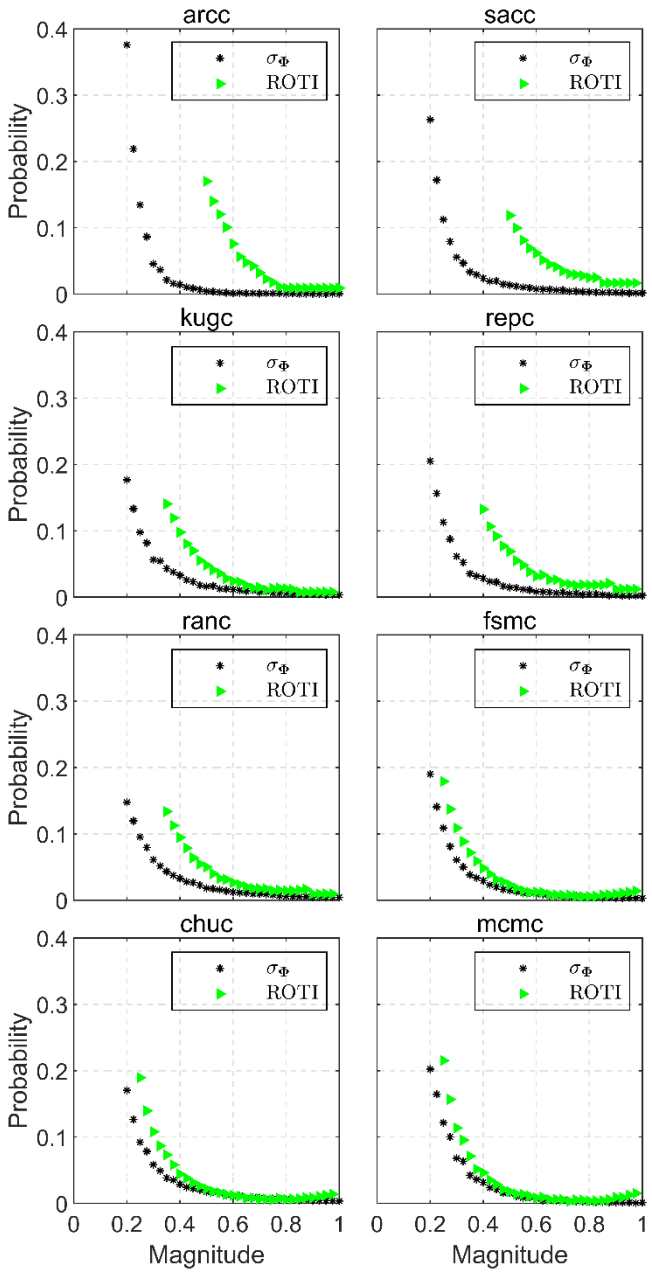

Fig. 15. Distribution of the scintillation index above the threshold.

The overall distribution does not ensure that ROTI can provide accurate magnitude of scintillation at the epoch level. To verify the magnitude accuracy of ROTI index derived from 30s-sampling-interval observation at the epoch level, the values of ROTI obtained at each station are divided into three classes ranging above the threshold with 0.2 TECU/min as the step. Then the distribution of σ_ϕ of the corresponding epochs in each class is analyzed. If ROTI can provide accurate scintillation at the epoch level, the distribution of the corresponding σ_ϕ should be concentrated in a certain interval above the threshold of σ_ϕ, and the median values of different intervals should increase with ROTI ranges.

Fig. 16 displays the overview of the distribution of σ_ϕ for different ranges of ROTI. In order to facilitate viewing, we have shifted the distribution of σ_ϕ for the first two ranges of ROTI along the positive direction of the x-axis by 0.2 and 0.4 respectively. The shifted distribution curves are denoted by dashed lines. This figure shows that for each ROTI range, the σ_ϕ is skewed distributed about the median, which is lower than its threshold. For low-latitude stations, such as mcmc, the proportion of σ_ϕ with large magnitude grows with the increase of ROTI, indicating that the accuracy of ROTI at the mcmc station is higher than those with higher latitudes. The median value of σ_ϕ does not increase significantly with the growth of the ROTI ranges, indicating that ROTI derived from 30s-sampling-interval observations cannot monitor scintillation accurately at the epoch level.

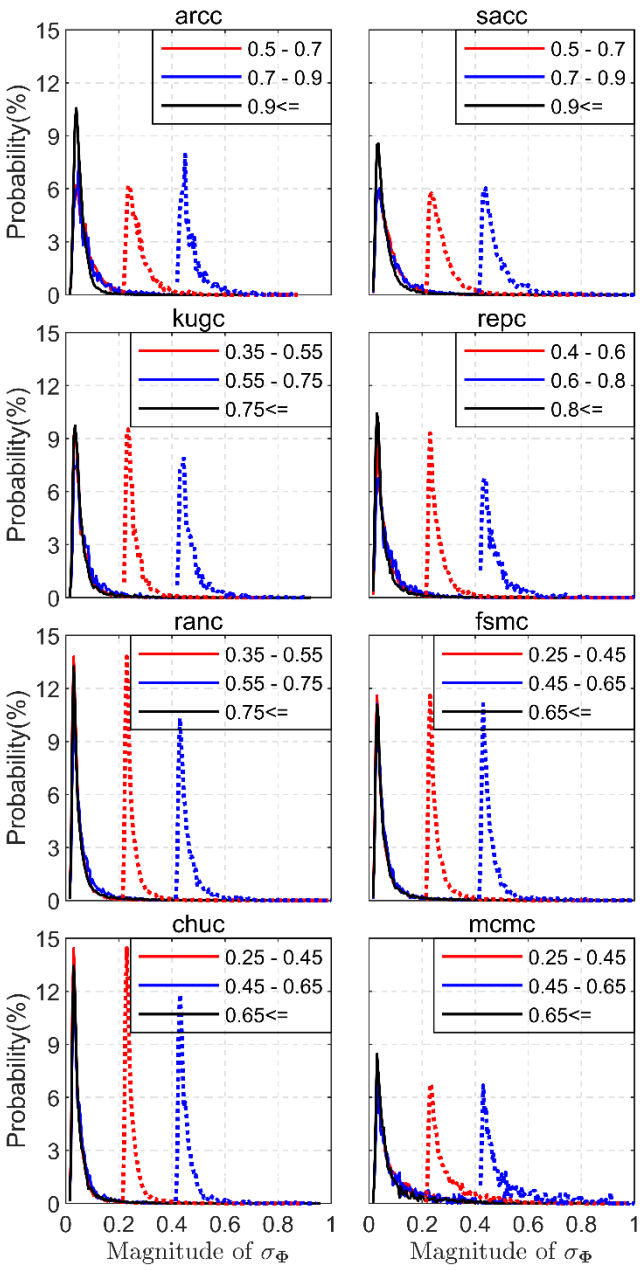

Fig. 16. Distribution of σ_ϕ for different ranges of ROTI. The numbers in legends denote the ranges of ROTI.

5. Discussion and conclusions

Most of the existing scintillation index researches are devoted to validating ROTI in the equatorial region using amplitude scintillation, which is rare in the polar region. To monitor the scintillation in the Arctic region continuously and extensively, it is important and efficient to utilize the existing widely distributed geodetic receivers recording observations at 30s-sampling-interval into the field of scintillation monitoring. In this study, we statistically analyzed the scintillation monitoring performance of ROTI extracted from 30s-sampling-interval observations through comparing to the phase scintillation index provided by ISMR based on data from 8 stations during a two-year-long period. The comparison in this paper mainly considered the following two aspects. The

first is the scintillation occurrence rate and its daily variation and correlation with different space weather parameters, while the second is the magnitude distribution.

Results of the detection scintillation occurrence rate from ROTI confirm that ROTI can monitor ionospheric scintillations accurately at all the 8 stations with the proposed thresholds. ROTI can also identify the most likely period within a day when scintillation events may occur in both normal and polar day/night periods. This result is similar to those obtained in the low-latitude (Basu et al. 2002; CERVERA et al. 2006) and polar regions (Jiao et al. 2013) using ISMR observations. The research results also confirm that the daily scintillation occurrence rate detected by ROTI only achieves a weak correlation at the polar cap region with the f10.7 index, while almost no correlation exists in other areas. A strong correlation can be obtained in the middle-high-latitude regions, but a weak correlation in the polar cap region for the global geomagnetic field index, e.g. Ap index. This result meets the existing research that high latitude ionospheric scintillations are mainly driven by the interplanetary magnetic field and magnetosphere processes, as discussed in the previous studies on the dependence of high-latitude scintillation occurrence on geomagnetic activities using observations from ISMR (Li et al. 2010; Alfonsi et al. 2011). The above discussion can conclude that ROTI has the scintillation detection capability at the hourly and pattern levels, and the detection capability in the middle-high-latitude region is higher than that in the polar cap region.

Results of the ionospheric scintillation magnitude distribution provided by ROTI reveal that the proportion of ionospheric scintillation with low magnitudes is significantly larger than that of high magnitude, while the distribution meets well with that given by ISMR, particularly in the middle-high-latitude region. This is consistent with most previous studies, indicating most scintillation events in the high-latitude region are relatively weak (Jiao et al. 2013). Results of the further classification of σ_ϕ based on different ranges of ROTI show that the median and the distances between the quartiles of σ_ϕ do not increase significantly with the growth of the ROTI ranges. With regards to the above analysis and the existing studies (Wei et al. 2019), it can conclude that accurate scintillation monitoring at the epoch level can be achieved in the ROTI index extracted from 1s-sampling-interval, instead of 30s-sampling-interval observations.

The preliminary study of this paper confirms that geodetic receivers with a sampling interval of 30s can serve as an alternative to ISMR by adopting ROTI as the scintillation index in the middle-high latitude region. This research offer promise for the future development of high-latitude ionospheric scintillation modelling and forecasting, through a more comprehensive analysis on the functional relationship between ROTI and σ_ϕ, the better knowledge of the scintillation occurrence frequency dependence on season and solar cycle, and an increasing number of GNSS stations. This can be a good candidate for the future extension of the current work.

Acknowledgments This study was supported by the Fundamental Research Funds for the Central Universities (2020QN30). We thank Joey Bernard from CHAIN for the personal emails confirming the clock failure. The F10.7 index is obtained from Natural Resources Canada. The historical Kp and Ap index are obtained from

German Research Centre for Geosciences. The ASY-H index and PCN index are obtained from Kyoto University and Technical University of Denmark respectively.

References

Aarons, J., 1982. Global morphology of ionospheric scintillations. Proc. IEEE 70(4), 360-378. Doi: 10.1109/PROC.1971.8122.

Ahmed, A., Tiwari, R., Strangeways, H., et al. 2015. Wavelet-based analogous phase scintillation index for high latitudes. Space Weather 13(8), 503-520. Doi: 10.1002/2015SW001183.

Alfonsi, L., Spogli, L., De Franceschi, G., et al., 2011. Bipolar climatology of GPS ionospheric scintillation at solar minimum. Radio Sci. 46(3): RS0D05. Doi: 10.1029/2010RS004571.

Alizadeh, M.M., Schuh, H., Zare, S., et al., 2020. Remote sensing ionospheric variations due to total solar eclipse, using GNSS observations. Geod. Geodynamics 11(3), 202-210. Doi: 10.1016/j.geog.2019.09.001.

Amabayo, E.B., Edward, J., Cilliers, P.J., et al., 2014. Climatology of ionospheric scintillations and TEC trend over the Ugandan region. Adv. Space Res. 53(5), 734-743. Doi: 10.1016/j.asr.2013.12.015.

ATıCı, R., SAĞıR, S., 2020. Global investigation of the ionospheric irregularities during the severe geomagnetic storm on September 7–8, 2017. Geod. Geodynamics 11(3), 211-221. Doi: 10.1016/j.geog.2019.05.004.

Basu, S., Groves, K.M., Basu, S., et al., 2002. Specification and forecasting of scintillations in communication/navigation links: current status and future plans. J. Atmos. Sol. Terr. Phys. 64(16), 1745-1754. Doi: 10.1016/S1364-6826(02)00124-4.

Béniguel, Y., Cherniak, I., Garcia-Rigo, A. et al., 2017. MONITOR Ionospheric Network: two case studies on scintillation and electron content variability. Ann. Geophys. 35, 377–391. Doi: 10.5194/angeo-35-377-2017.

Bhattacharyya, A., Beach, T.L., Basu, S., et al., 2000. Nighttime equatorial ionosphere: GPS scintillations and differential carrier phase fluctuations. Radio Sci. 35(1), 209-224. Doi: 10.1029/1999RS002213.

Carrano, C.S., Groves, K.M., Rino, C.L., 2019. On the relationship between the rate of change of total electron content index (ROTI), irregularity strength (CkL), and the Scintillation Index (S4). J. Geophys. Res. Space Phys. 124(3), 2099-2112. Doi: 10.1029/2018JA026353.

Cervera, M.A., Thomas, R.M., 2006. Latitudinal and temporal variation of equatorial ionospheric irregularities determined from GPS scintillation observations. Ann. Geophys. 24(12), 3329-3341. Doi: 10.5194/angeo-24-3329-2006.

Cherniak, I., Krankowski, A., Zakharenkova, I., 2018. ROTI Maps: a new IGS ionospheric product characterizing the ionospheric irregularities occurrence. GPS Solut. 22(3), 69. Doi: 10.1007/s10291-018-0730-1.

Clauer, C.R., McPherron, R.L. 1980. The relative importance of the interplanetary electric field and magnetospheric substorms on partial ring current development. J. Geophys. Res. 85(A12), 6747-6759. Doi: 10.1029/JA085iA12p06747.

Crooker, N.U., 1972. High-time resolution of the low-latitude asymmetric disturbance in the geomagnetic field. J. Geophys. Res. 77(4), 773-775. Doi: 10.1029/JA077i004p00773.

Davis, T.N., Sugiura, M., 1966. Auroral electrojet activity index AE and its universal time variations. J. Geophys. Res., 71(3), 785-801. Doi: 10.1029/JZ071i003p00785.

Dugassa, T., Habarulema, J.B., Nigussie, M., 2019. Longitudinal variability of occurrence of ionospheric irregularities over the American, African and Indian regions during geomagnetic storms. Adv. Space Res. 63(8), 2609-2622. Doi: 10.1016/j.asr.2019.01.001.

Fabbro, V., Jacobsen, K.S., Rougerie, S., 2019. HAPEE, a statistical approach for ionospheric scintillation prediction in the polar region. In proceedings of the Beacon Satellite Symposium, OLSZTYN, Poland, August 2019, hal-02365033.

Jayachandran, P., Langley, R., Macdougall, J., et al., 2009. Canadian high arctic ionospheric network (CHAIN). Radio Sci. 44(1), 1-10. Doi: 10.1029/2008RS004046.

Jiao, Y., Morton, Y.T., 2015. Comparison of the effect of high-latitude and equatorial ionospheric scintillation on GPS signals during the maximum of solar cycle 24. Radio Sci. 50(9), 886-903. Doi: 10.1002/2015RS005719.

Jiao, Y., Morton, Y.T., Taylor, S., et al., 2013. Characterization of high-latitude ionospheric scintillation of GPS signals. Radio Sci. 48(6), 698-708. Doi: 10.1002/2013RS005259.

Jin, Y., Moen, J.I., Miloch, W.J., 2014. GPS scintillation effects associated with polar cap patches and substorm auroral activity: direct comparison. J. Space Weather Space Clim. 4, A23. Doi: 10.1051/swsc/2014019.

Juan, J.M., Aragon-Angel, A., Sanz, J., et al., 2017. A method for scintillation characterization using geodetic receivers operating at 1 Hz. J. Geod. 91(11), 1383-1397. Doi: 10.1007/s00190-017-1031-0.

Juan, J.M., Sanz, J., Rovira-Garcia, A., et al., 2018. AATR an ionospheric activity indicator specifically based on GNSS measurements. J. Space Weather Space Clim., 8, A14. Doi: 10.1016/j.jastp.2020.105254.

Karatay, S., 2020. Temporal variations of the ionospheric disturbances due to the seasonal variability over Turkey using IONOLAB-FFT algorithm. Geod. Geodynamics 11(3), 182-191. Doi: 10.1016/j.geog.2019.12.002.

Khazanov, G.V., (Ed.). 2016. Space weather fundamentals. 1st edn. CRC Press, Boca Raton, USA.

Kintner, P.M., Ledvina, B.M., De Paula, E., 2007. GPS and ionospheric scintillations. Space Weather 5(9), 1-23. Doi: 10.1029/2006SW000260.

Li, G., Ning, B., Ren, Z., et al., 2010. Statistics of GPS ionospheric scintillation and irregularities over polar regions at solar minimum. GPS Solut. 14(4), 331-341. Doi: 10.1007/s10291-009-0156-x.

Li, G., Ning, B., Wang, C. et al., 2018. Storm-enhanced development of postsunset equatorial plasma bubbles around the meridian 120°E/60°W on 7–8 September 2017. J. Geophys. Res. Space Phys. 123(9), 7985-7998. Doi: 10.1029/2018JA025871.

Luo, X., Gu, S., Lou, Y., et al., 2020. Amplitude scintillation index derived from C/N0 measurements released by common geodetic GNSS receivers operating at 1 Hz. J. Geod. 94(2), 27. Doi: 10.1007/s00190-020-01359-7.

Ma, G., Maruyama, T., 2006. A super bubble detected by dense GPS network at east Asian longitudes. Geophys. Res. Lett. 33(21), 103. Doi: 10.1029/2006GL027512.

Matzka, J., Stolle, C., Yamazaki, Y., et al., 2021. The geomagnetic Kp index and derived indices of geomagnetic activity. Space Weather 19:e2020SW002641. Doi: 10.1029/2020SW002641.

Meeus, J., 1998. Astronomical Algorithms, 2nd edn. Willmann-Bell, Inc., Richmond, Virginia, USA.

Nguyen, V.K., Rovira-Garcia, A., Juan, J.M., et al., 2019. Measuring phase scintillation at different frequencies with conventional GNSS receivers operating at 1 Hz. J. Geod. 93(10), 1985-2001. Doi: 10.1007/s00190-019-01297-z.

Olwendo, J.O., Cilliers, P., Weimin, Z., et al., 2018. Validation of ROTI for ionospheric amplitude scintillation measurements in a low-latitude region over Africa. Radio Sci. 53(7), 876-887. Doi: 10.1029/2017RS006391.

Pi, X., Mannucci, A.J., Lindqwister, U.J., et al., 1997. Monitoring of global ionospheric irregularities using the Worldwide GPS Network. Geophys. Res. Lett. 24(18), 2283-2286. Doi: 10.1029/97GL02273.

Pi, X., Mannucci, A.J., Valant-Spaight, B., et al., 2013. Observations of global and regional ionospheric irregularities and scintillation using GNSS tracking networks. In proceedings of the ION 2013 Pacific PNT Meeting, Honolulu, Hawaii, April 2013, pp. 752-761.

Prikryl, P., Jayachandran, P. T., Mushini, S. C., et al. 2015. Climatology of GPS phase scintillation at northern high latitudes for the period from 2008 to 2013. Ann. Geophys. 33, 531–545. Doi: 10.5194/angeo-33-531-2015.

Priyadarshi, S., Zhang, Q.H., Ma, Y., et al., 2018. The behaviors of ionospheric scintillations around different types of nightside auroral boundaries seen at the Chinese Yellow River Station, Svalbard. Front. Astron. Space Sci. 5, 26. Doi: 10.3389/fspas.2018.00026.

van der Meeren, C., Oksavik, K., Lorentzen, D.A., et al., 2015. Severe and localized GNSS scintillation at the poleward edge of the nightside auroral oval during intense sub-storm aurora. J. Geophys. Res. Space Phys. 120, 10607–10621. Doi: 10.1002/2015JA021819.

Van Dierendonck, A.J., Klobuchar, J., Hua, Q., 1993. Ionospheric scintillation monitoring using commercial single frequency C/A code receivers. In proceedings of ION GPS 1993. Institute of Navigation, Salt Lake City, UT, September 1993, pp. 1333-1342.

Vani, B.C., Shimabukuro, M.H., Galera Monico, J.F., 2017. Visual exploration and analysis of ionospheric scintillation monitoring data: The ISMR Query Tool. Computers Geosciences 104, 125-134. Doi: 10.1016/j.cageo.2016.08.022.

Wei, W., Li, W., Song S., et al., 2019. Study on the calculation strategies of ionospheric scintillation index ROTI from GPS. In proceedings of 2019 IEEE International Geoscience and Remote Sensing Symposium, Yokohama, Japan, 28 July-2 Aug. 2019, pp. 9894-9897.

Xiong, J., Han, F., 2020. Positioning performance analysis on combined GPS/BDS precise point positioning. Geod. Geodynamics 11(1), 78-83. Doi: 10.1016/j.geog.2019.11.001.

Yang, Z., Liu, Z., 2016. Correlation between ROTI and Ionospheric Scintillation Indices using Hong Kong low-latitude GPS data. GPS Solut. 20(4), 815-824. Doi: 10.1007/s10291-015-0492-y.

Yizengaw, E., Groves, K.M., 2018. Longitudinal and seasonal variability of equatorial ionospheric irregularities and electrodynamics. Space Weather 16(8), 946-968. Doi: 10.1029/2018SW001980.

Zhao, D., Hancock, C.M., Roberts, G.W., et al., 2019a. Cycle slip detection during high ionospheric activities based on combined triple-frequency GNSS signals. Remote Sens. 11(3), 250. Doi: 10.3390/rs11030250.

Zhao, D., Li W., Li C., et al., 2021. Extracting an ionospheric phase scintillation index based on 1 Hz GNSS observations and its verification in the Arctic region. Acta Geod. Cartographica Sinica 50(3), 368-383. Doi: 10.11947/j.AGCS.2021.20200454.

Zhao, D., Roberts, G.W., Hancock, C.M., et al., 2019b. A triple-frequency cycle slip detection and correction method based on modified HMW combinations applied on GPS and BDS. GPS Solut. 23(1), 22. Doi: 10.1007/s10291-018-0817-8.